

Supporting Information for

**Liquid plasticine: controlled deformation and recovery of
droplet with interfacial nanoparticle jamming**

Xiaoguang Li,^{*,a} Yahui Xue,^b Pengyu Lv,^b Hao Lin,^c Feng Du,^b Yueyun Hu,^a

Jun Shen,^{*,a} and Huiling Duan^{*,b}

^aShanghai Key Laboratory of Special Artificial Microstructure Materials and Technology, School of Physics Science and Engineering, Tongji University, Shanghai 200092, China.

^bState Key Laboratory for Turbulence and Complex Systems, Center for Applied Physics and Technology, Department of Mechanics and Engineering Science, College of Engineering, Peking University, Beijing 100871, China.

^cMechanical and Aerospace Engineering, Rutgers, The State University of New Jersey, New Jersey 08854, USA

Contents:

Figure S1. Schematic of Experimental setup for droplet squeezing with controllable forces.

Figure S2. Characterization of the silica coating on glass substrate.

Figure S3. 3D images of deformed droplets reconstructed by the Matlab method.

Figure S4. Series of Matlab images of a deformed droplet during injection.

Figure S5. Photographs and reconstructed 3D images of naked droplets under gravity.

Figure S6. Comparison of predicted and experimental surface area-volume (S-V) relations for naked droplets.

Figure S7. Photographs of big liquid plasticine.

Figure S8. Direct voltage-induced flow phenomena in liquid plasticine.

Figure S9. The cutting of liquid plasticine.

Theoretical derivations

1. Surface area-volume relation for sessile droplets under gravity
2. Nanoparticle interactions at water surface
3. Capillary pressure between nearby nanoparticle
4. Reference

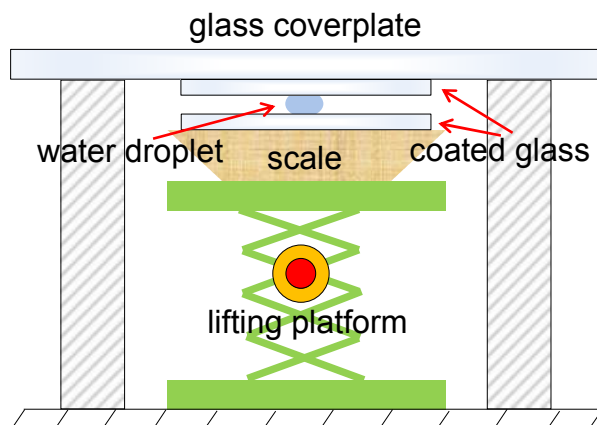


Figure S1. Schematic of experimental setup for droplet squeezing with controllable forces. The base (the lower coated glass) carrying a droplet is put on an electronic scale on a lifting platform. The tool (the upper coated glass) is stuck on a thick glass whose position is fixed. By adjusting the height of the lifting platform, the force applied on the droplet is controlled and is shown by the scale (working range: 0.1 mN-5 N; resolution: 0.01 g).

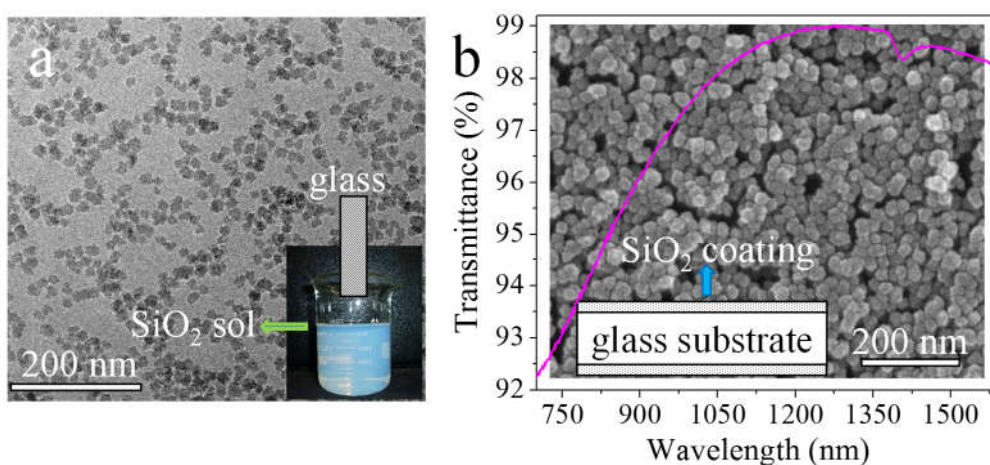


Figure S2. Characterization of the silica coating on glass substrate. (a) Transmission electron microscopy (TEM) image of the sol that consists of SiO_2 particles of ~ 20 nm. The inset is a picture of the SiO_2 sol and the schematic of dip-coating. (b) Transmittance spectrum of the glass with the sol-gel coating and its scanning electron microscopy (SEM) morphology; the observed particle size is larger than the true value due to the platinum spraying treatment. The inset sketches the coated glass after dip-coating. This porous coating increased the transmittance of glass from $\sim 92.0\%$ to $\sim 99.0\%$ by reducing the Fresnel reflection. That's to say, this coating is both superhydrophobic and antireflective, with the particles removed easily.

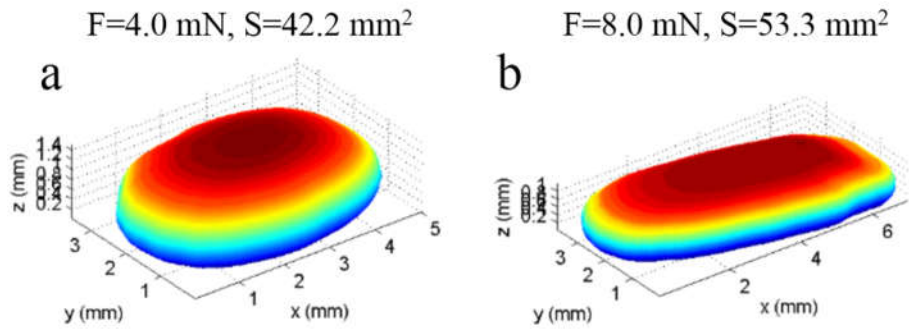


Figure S3. 3D images of deformed droplets reconstructed by the Matlab method. Two squeezing forces (i.e. $F = 4.0$ and 8.0 mN) are chosen here as an example. The droplet volume is $20 \mu\text{l}$ for both (a) and (b), and the surface areas are calculated as 42.2 mm^2 for $F=4.0$ mN and 53.3 mm^2 for $F=8.0$ mN, respectively.

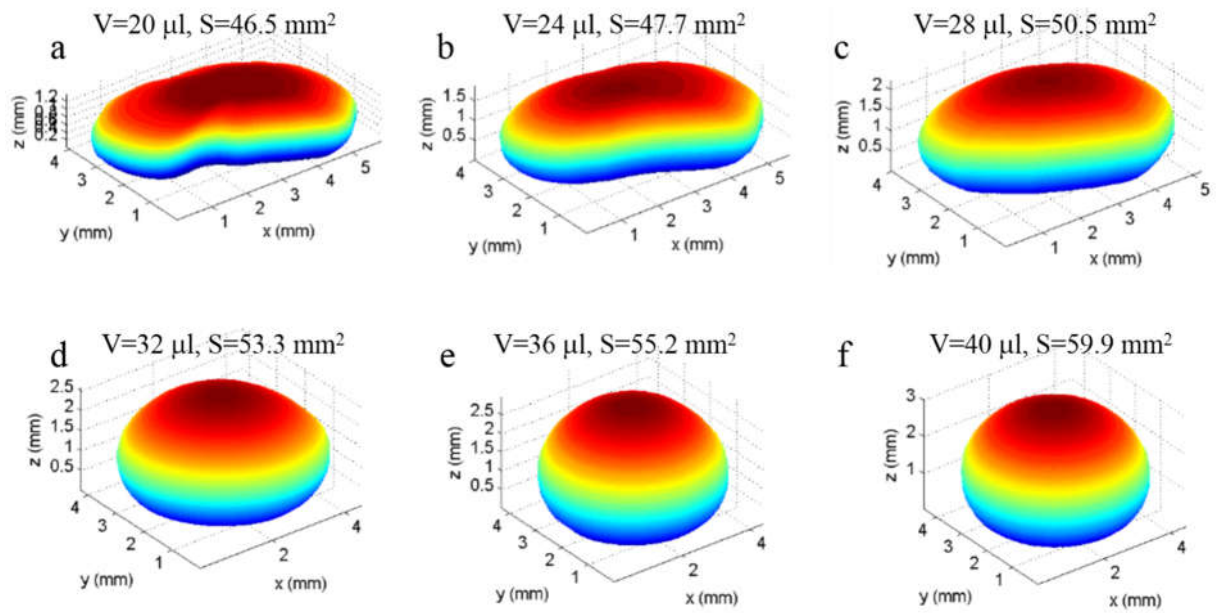


Figure S4. Series of Matlab images of a deformed droplet during injection. The droplet of $20 \mu\text{l}$ was initially squeezed under $F = 6$ mN as an example. The total volume and surface area at each injection stage are marked, respectively.

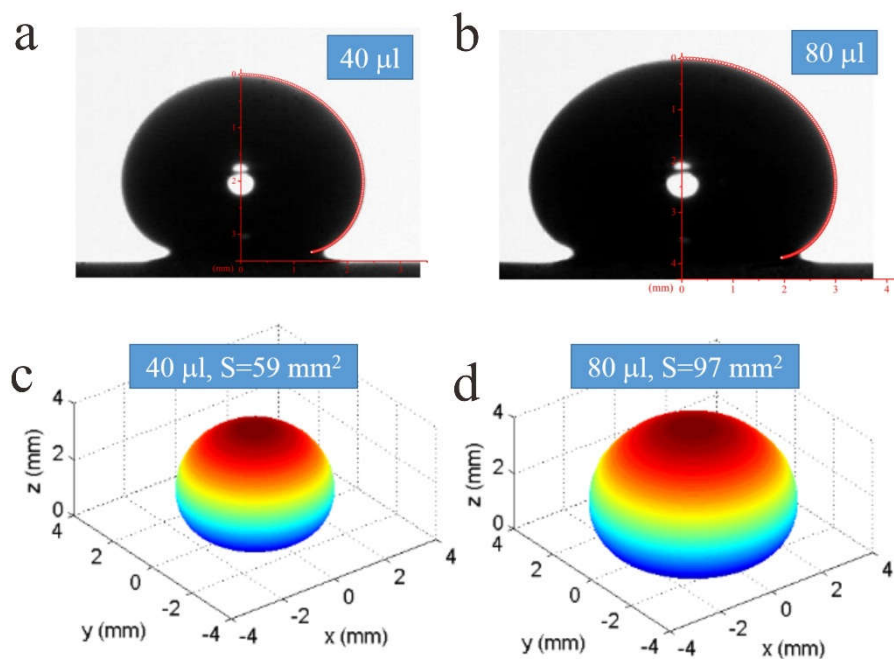


Figure S5. Photographs and reconstructed 3D images of naked droplets under gravity. (a) and (b) are side views of 40 and 80 μl naked droplets. The red curves correspond to the theoretical results which agree well with the experimental images. (c) and (d) are reconstructed 3D images by the Matlab method according to (a) and (b), respectively.

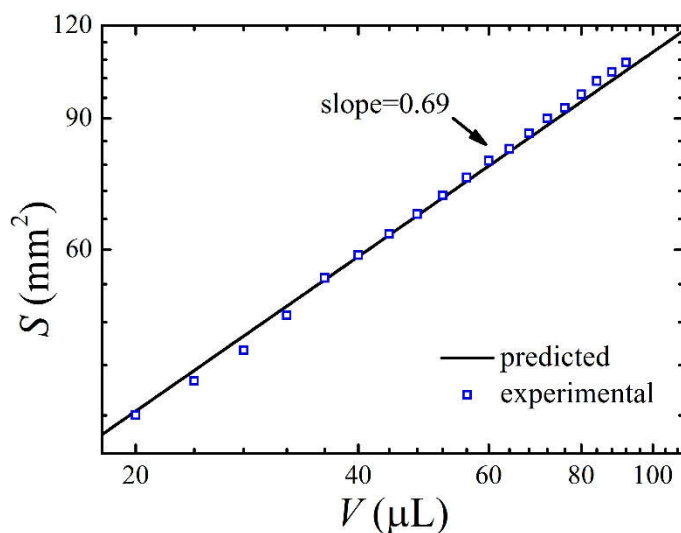


Figure S6. Comparison of predicted and experimental surface area (S)-volume (V) relations for naked droplets. The numerical results are calculated according to Equations S3 and S4 below. The experimental results are obtained by 3D image reconstruction method.

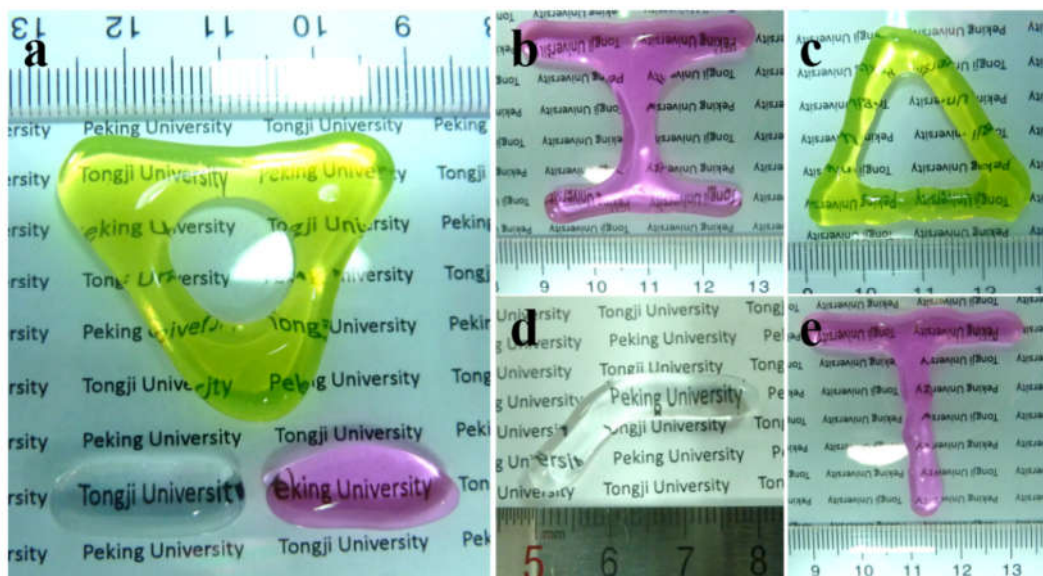


Figure S7. Photographs of big liquid plasticine. Both pure (d) and dyed water were employed for this experiment. The light green droplet in (a) was obtained by injecting water into the one in (c).

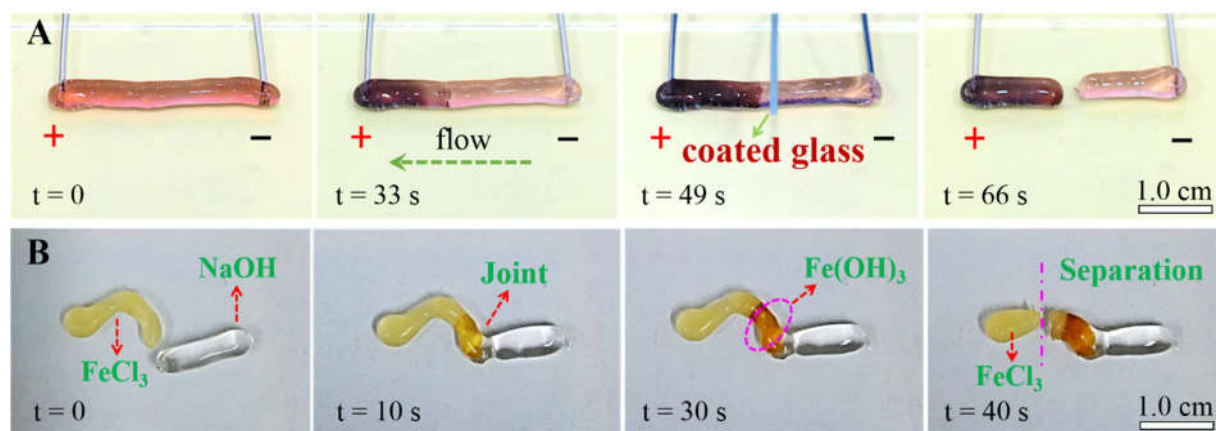


Figure S8. Diffusion in liquid plasticine. (A) Electrophoresis of a hydrosol of nanogold particles (~ 20 nm, Au concentration of 330 ppm) in a linear droplet. The voltage was maintained as 30 V. Similar to what is presented in the manuscript, the converging of Au nanoparticles to the left resulted in the color change. (B) Chemical reaction of FeCl_3 (1 mol/L) and NaOH (3 mol/L) with two deformed droplets. As shown, after the two droplets were jointed the chemical reaction began which was reflected by the color change, but proceeded much slower compared with the case of mixing two normal droplets (see Ref 18 in the manuscript); this was mainly because that the elongated shape restricted the diffusion. Both of (A) and (B) illustrate the channel function of liquid plasticine, and demonstrate that different parts with different properties can be separated easily by the cutting. Experiment B also demonstrates the reactor function.

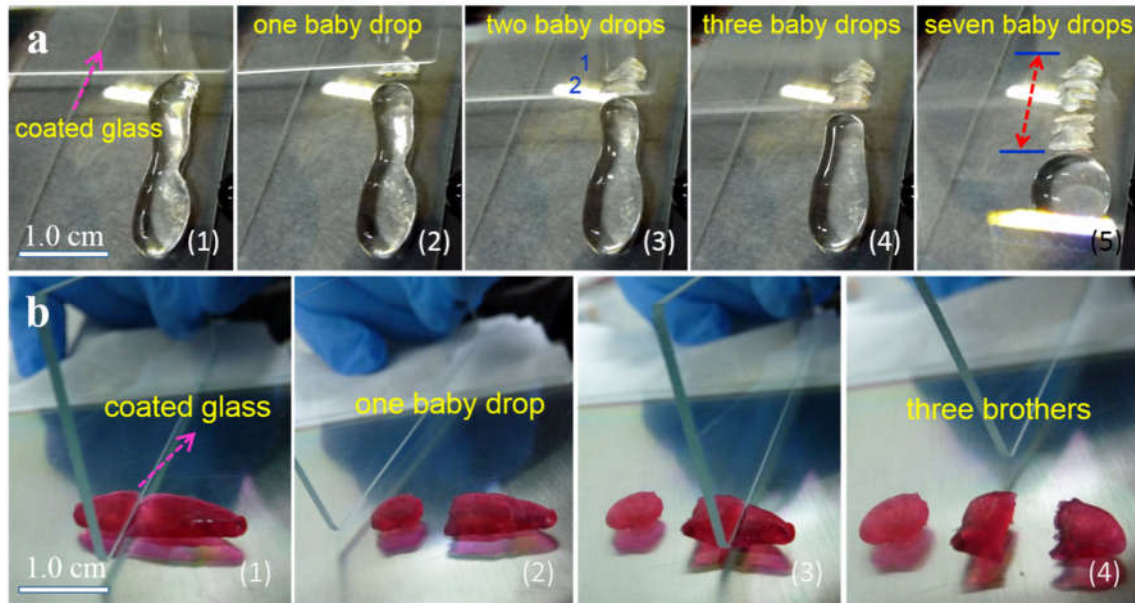


Figure S9. The cutting of liquid plasticine. Pure (a) and dyed (b) linear droplets were prepared for the cutting demonstration. As shown, the plasticine can be cut into several parts easily using a hydrophobic knife (coated glass is employed here) and the size choice is almost at will.

Theoretical derivations

1. Surface area-volume relation for sessile droplets under gravity

The shape of a sessile droplet under gravity on a flat surface (Figure S10) is governed by the balance between the Laplace pressure and gravity, that is^[1]

$$\gamma \left[\frac{z''(x)}{(1+z'(x)^2)^{3/2}} + \frac{z'(x)}{x(1+z'(x)^2)^{1/2}} \right] = \frac{2\gamma}{b} + \rho g z(x) \quad (\text{S1})$$

where γ is liquid surface tension, ρ is density, g is gravity acceleration, and b is half the curvature radius at the apex (point O).

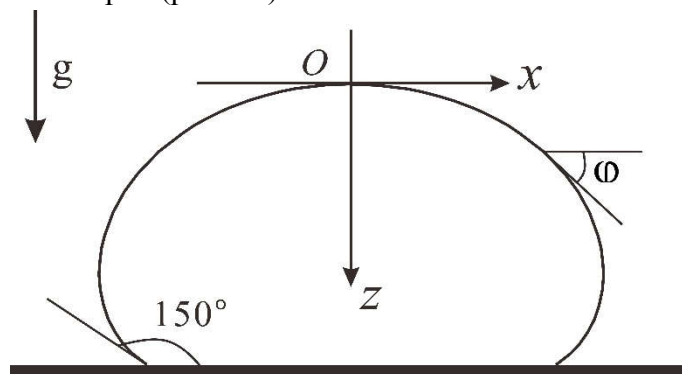


Figure S10. Side view of a sessile droplet under gravity on a flat surface.

By introducing φ as an intermediate variable, we may rewrite Equation S1 as

$$x'(\varphi) = \frac{\gamma \cos \varphi}{-\gamma \sin \varphi / \sin \varphi + 2\gamma/b + \rho g z(\varphi)} \quad (\text{S2})$$

$$z'(\varphi) = x'(\varphi) \tan \varphi$$

with boundary conditions: $x(\varphi)=0$ and $z(\varphi)=0$ at $\varphi=0$. The parameter (b) is determined by the condition of volume conservation. For given b , numerically solving Equation S2 would result in the shape of a sessile droplet under gravity, which agrees well experiment observations (Figure S5). Then, the total surface area (including liquid-vapor and solid-liquid interfaces) and volume of the sessile droplet can be obtained by the following integrations, respectively,

$$S = \int_0^\theta 2\pi x(\varphi)x'(\varphi)/\cos \varphi d\varphi + \pi x(\theta)^2 \quad (\text{S3})$$

$$V = \int_0^\theta \pi x(\varphi)^2 x'(\varphi) \tan \varphi d\varphi \quad (\text{S4})$$

where θ is contact angle and equals 150° here. The first term on the right hand side of Equation S3 is the liquid-vapor interface area, and the second term is the solid-liquid interface area. By using data, $\gamma=0.0728$ N/m for water and $g = 9.8$ N/Kg, we calculated the variation of the total surface area (S) versus the volume (V) of sessile droplets under gravity. It shows a power-law relation between S and V with the power exponent equal to 0.69 (Figure S6), that is,

$$S \sim V^{0.69} \quad (\text{S5})$$

This coefficient (0.69) is slightly higher than that (i.e. 2/3) for a spherical droplet with neglected gravity.

2. Nanoparticle interactions at water surface

The particle assembly at the water-air interface is dominated by particle-particle interactions, which include the capillary force, van der Waals attraction, screened-Coulomb repulsion, and dipole-dipole repulsion.^[2,3] Whereas the capillary interaction energy is much smaller than the thermal energy when the radius is far less than $\sim 10 \mu\text{m}^{[5]}$, the interaction between silica nanoparticles is generally controlled by the van der Waals and electrostatic interactions (see 2.1, 2.2, 2.3 in the below). The total particle-particle interaction energy, U_{tot} , normalized by $k_{\text{B}}T$ (where k_{B} is Boltzman constant and T is temperature), is expressed as:

$$\frac{U_{\text{tot}}}{k_{\text{B}}T} = \frac{U_{\text{vdW}}}{k_{\text{B}}T} + \frac{U_{\text{dipole}}}{k_{\text{B}}T} + \frac{U_{\text{coulomb}}}{k_{\text{B}}T} \quad (\text{S6})$$

The vdW attraction exists for the whole part of each particle, while the electrostatic repulsion only exists between the immersed parts since surface ionization happens at the silica-water interface (schematic 1 in Figure S11A). Thus, the immersed height

fraction α of those particles significantly affects their interaction strength. The plots of $U_{\text{tot}}/k_B T$ as a function of particle gap, $\delta (= d-2r$, where d is center-to-center distance and r is particle radius), for six different values of α , are shown in Figure S11B. A potential barrier exists for $\alpha > 15\%$, which approaches infinity as α gets close to one. The barrier means that particles tend to bond together when their gap is less than the barrier position, in which case, the vdW attraction is dominant. In addition, for stacked particles (schematic 2 in Figure S11A) which may occur according to the mechanism shown in Figure 1F, they are equivalent to a bigger particle with a smaller immersed height fraction.

Thus, forcing particles close enough (several nanometers apart) causes the formation of a stable solid film, and this is the microscopic mechanism of particle jamming. The small gaps between those closely packed nanoparticles could provide high capillary pressure difference, and thus help the particle film withstand high liquid pressure without leakage (see the third part of Theoretical derivation). When jamming is relieved, as the corresponding cases described in Figure 3B, the electrostatic repulsion gradually dominates, and this helps to form the particle islands with the injection manipulation.

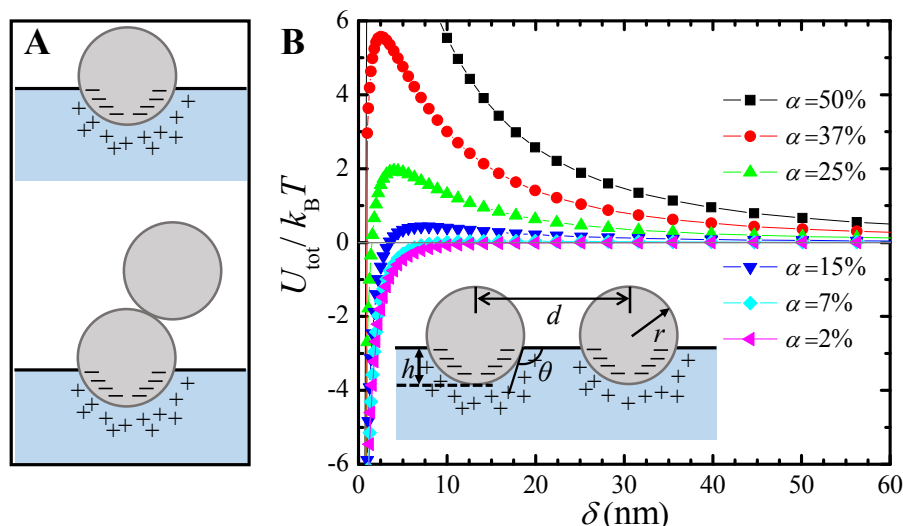


Figure S11 Energy analysis of the compound interface of deformed droplet. (A) Separate schematics of single particle and stacked particle attachments. (B) Total particle-particle interaction energy, U_{tot} , (normalized by $k_B T$) versus particle gap. The inset is a schematic of two adjacent nanoparticles partially immersed in a water droplet. Here, h is immersion depth, and α is immersion fraction and equals $h/2r$, where r is particle radius. The subaqueous parts are endowed with double electric layers, which generate electrostatic repulsion between particles.

2.1 Capillary interaction

The capillary interaction energy between floating spheres of radius r at a horizontal center-to-center distance, d , can be expressed as^[4]

$$U_{\text{cap}} = -2\pi\gamma r^2 B^2 S^2 K_0(d/a) \quad (\text{S7})$$

where a is the capillary length, B is the Bond number, and

$$S = \frac{2}{3} \frac{\rho_s}{\rho} - \frac{1}{3} - \frac{1}{2} \cos \theta + \frac{1}{6} \cos^3 \theta$$

Here, ρ_s and ρ are sphere and water densities, respectively, and θ is contact angle (Figure S12). For silica sphere particles, $\rho_s/\rho = 2.6$. The capillary length is defined by $a = (\gamma/\rho g)^{1/2}$, and the Bond number is defined by $B = (r/a)^2$. Given $\theta = 105^\circ$ for hydrophobic silica particles, the variation of U_{cap} , as normalized by the thermal energy $k_B T$, with r at $d = 2r$ is plotted in Figure S13. It is seen that when the radius is much smaller than $\sim 6 \mu\text{m}$, the capillary interaction energy is much smaller than the thermal energy and thus negligible.

Nevertheless, the particles trapped at the water-air interface are thermodynamically stable since the detachment energy for each particle, expressed by^[5]

$$U_{\text{remove}} = \pi r^2 \gamma (1 + \cos \theta)^2 \quad (\text{S8})$$

reaches as high as 3000-fold of $k_B T$ even for particles of radius $r = 10 \text{ nm}$. This indicates that once attached at the water surface, those nanoparticles can hardly be removed.

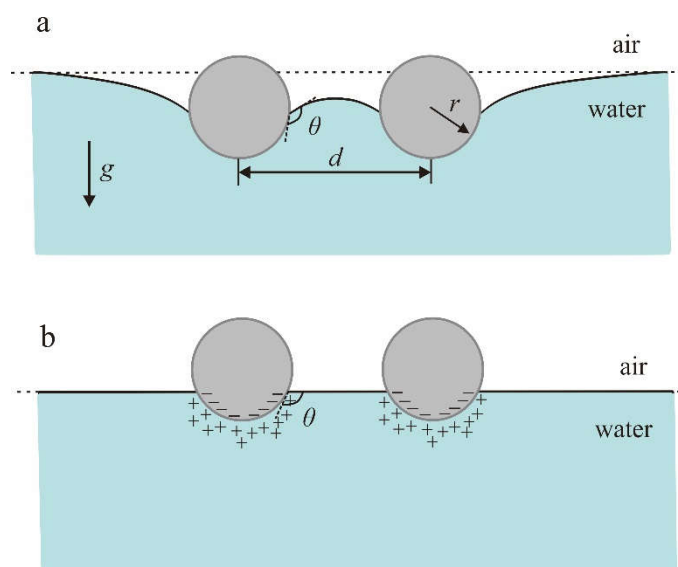


Figure S12. Schematic of particles trapped at the water-air interface. (a) For larger particles, the deformed water-air interface due to gravitation causes significant capillary interaction between particles. (b) For smaller particles, the meniscus is undeformed and the particle-particle interaction is controlled by the van der Waals and electrostatic interactions.

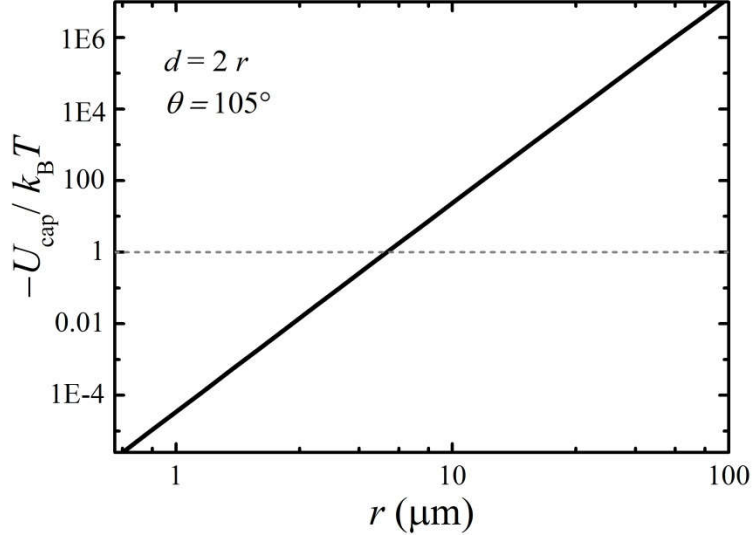


Figure S13. Variation of capillary interaction energy between particles with the radius.

2.2. Van der Waals interaction

The van der Waals (vdW) interaction energy between equal spheres partially immersed at the water-air interface is given by^[6-8]

$$U_{\text{vdW}} = -\frac{A_{\text{eff}}}{6} \left[\frac{2r^2}{d^2 - 4r^2} + \frac{2r^2}{d^2} + \ln \frac{d^2 - 4r^2}{d^2} \right] \quad (\text{S9})$$

where A_{eff} is the effective Hamaker constant,

$$A_{\text{eff}} = A_{\text{pp}} + \alpha^2(3 - 2\alpha)(A_{\text{pwp}} - A_{\text{pp}}) \quad (\text{S10})$$

Here, α is the immersed height fraction and equals $(1 + \cos\theta)/2$, A_{pp} is the Hamaker constant for the particles in vacuum, and A_{pwp} is the effective bulk Hamaker constant for the particles in the water. For silica, $A_{\text{pp}} = 6.35 \times 10^{-20}$ J, and $A_{\text{pwp}} = 0.48 \times 10^{-20}$ J^[9]. In the calculation below, λ is taken as 100 nm.

2.3. Electrostatic interaction

The electrostatic interaction between partially immersed particles at the water-air interface includes two parts, the dipole-dipole interaction and screened-Coulomb interaction. Their respective interaction energy are expressed as^[10, 11]

$$U_{\text{dipole}} = \frac{2q^2}{4\pi\epsilon_0(\epsilon\kappa)^2 d^3} \quad (\text{S11})$$

and

$$U_{\text{coulomb}} = \frac{2q^2}{4\pi\epsilon_0\epsilon d} \frac{\epsilon^2}{\epsilon^2 - 1} \exp[-\kappa d] \quad (\text{S12})$$

where ϵ_0 is the permittivity of vacuum, ϵ is the relative permittivity of water, κ is the reciprocal of the Debye screening length, and q is the charge of the water-immersion section of the particle. Here, $\epsilon_0 = 8.85 \times 10^{-12}$ F/m, $\epsilon = 80$, and $\kappa^{-1} = 0.7 \mu\text{m}$ ^[10]. When r is much smaller than κ^{-1} , $q = 2\pi r^2(1 + \cos\theta)\sigma$, where σ is the particle surface charge

density due to surface dissociation. The unknown parameter of σ is taken as $\sigma = -1$ mC/m²[12], typical value for ionized silica surfaces in water.

3. Capillary pressure between nearby nanoparticles

The transformation of the liquid–vapor interface among three nearby particles under different liquid pressure is described by the Laplace equation,

$$P_c = \frac{2\gamma \cos \varphi}{r_c} \quad (\text{S13})$$

where P_c is the pressure difference across the meniscus, r_c is the effective capillary radius in the order of particle size, and φ is the transformation angle of the meniscus. For a droplet, the maximum height tends to twice the capillary length, a , that is, $H_{\max} = 2a$. This yields a maximum liquid pressure P_{\max} in the water puddle:

$$p_{\max} = \rho g H_{\max} = 2\rho g a \quad (\text{S14})$$

The maximum φ can be calculated by equating Eqs. (S12) and (S13). Taking $r_c = 10$ nm yields a value of φ very close to 0 (see Figure S12). This indicates that the deformation of the meniscus after the change in droplet shape is negligible. On the other hand, the liquid–vapor interfacial area, S_{LV} , remains almost constant for various deformations, and thus, the total free energy of the droplet system varies negligibly for different deformations. A deformed droplet will therefore not change spontaneously to form other shapes, and the various deformations are all stable. This reflects the stability of single deformed droplet and water art.

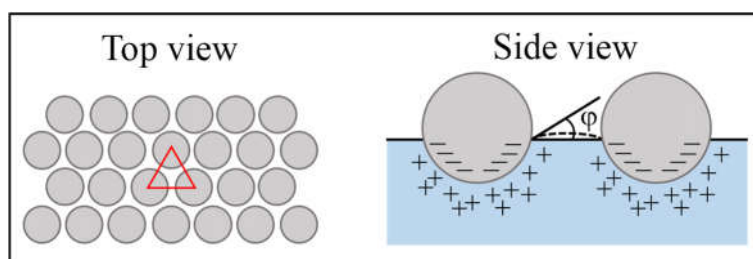


Figure S14. Schematic of close triangular arrangement of nanoparticles.

Reference:

- [1] Hiemenz, P. C.; Rajagopalan, R. Principles of Colloid and Surface Science, 3rd ed.; CRC Press: New York, 1997.
- [2] Hunter, T. N., Pughb, R. J., Franksc, G. V., Jamesona, G. J., Adv. Colloid. Interface. Sci. 2008, 137, 57-81.
- [3] Bresme, F., Oettel, M., J. Phys-Condens. Mat. 2007, 19, 413101.
- [4] Chan, D.Y.C., J.D. Henry, and L.R. White, The Interaction of Colloidal Particles

- Collected at Fluid Interfaces. *Journal of Colloid and Interface Science*, 1981. 79(2): p. 410-418.
- [5] Kralchevsky, P.A. and K. Nagayama, Capillary interactions between particles bound to interfaces, liquid films and biomembranes. *Advances in Colloid and Interface Science*, 2000. 85(2-3): p. 145-192.
- [6] Gregory, J. (1981). Approximate expressions for retarded van der Waals interaction. *Journal of Colloid and Interface Science*, 83(1), 138-145.
- [7] Williams, D.F. and J.C. Berg, The Aggregation of Colloidal Particles at the Air-Water-Interface. *Journal of Colloid and Interface Science*, 1992. 152(1): p. 218-229.
- [8] van de Ven, T.G.M. *Colloidal Hydrodynamics* (Academic Press, Sandiego, CA, 1989).
- [9] Bergstrom, L., Hamaker constants of inorganic materials. *Advances in Colloid and Interface Science*, 1997. 70: p. 125-169.
- [10] Hurd, A.J., The Electrostatic Interaction between Interfacial Colloidal Particles. *Journal of Physics a-Mathematical and General*, 1985. 18(16): p. 1055-1060.
- [11] Aveyard, R., et al., Measurement of Long-Range Repulsive Forces between Charged Particles at an Oil-Water Interface. *Physical Review Letters*, 2002. 88(24).
- [12] Behrens, S.H. and D.G. Grier, The charge of glass and silica surfaces. *The Journal of Chemical Physics*, 2001. 115(14): p. 6716.